Korean J. Chem. Eng., 40(7), 1587-1597 (2023)
DOI: 10.1007/s11814-023-1430-2

pISSN: 0256-1115
eISSN: 1975-7220

Influence of gas exhaust geometry on flow pattern, performance, and erosion rate of a gas cyclone

Farzad Parvaz*, Seyyed Hossein Hosseini,†, Ahmad Reza Bastan**, Jamal Foroozesh***, Nihan Uygur Babaoğlu****, Khairy Elsayed*****,******, and Goodarz Ahmadi*******

*Department of Mechanical Engineering, Semnan University, P.O. Box 35131-191, Semnan, Iran
**Department of Chemical Engineering, Ilam University, Ilam 69315-516, Iran
***Department of Metallurgy and Materials Science, Faculty of Engineering,
Shahid Bahonar University of Kerman, Kerman, Iran
****Department of Environmental Engineering, Kahramanmaras Sutcu Imam University, Kahramanmaras, Turkey
*****Mechanical Power Engineering Department, Faculty of Engineering at El-Mattaria,
Helwan University, Masaken El-Helmia P.O., Cairo 11718, Egypt
******Mechanical Engineering Department, College of Engineering and Technology-Smart Village Campus,
Arab Academy for Science, Technology and Maritime Transport (AASTMT), P.O. Box 12676, Giza, Egypt
*******Department of Mechanical and Aerospace Engineering, Clarkson University, Potsdam, NY 13699-5725, USA
(*Received 9 October 2022 • Revised 20 January 2023 • Accepted 13 February 2023*)

Abstract−The effect of gas exhaust shape on the performance, flow pattern, and erosion rate of a gas cyclone was investigated using a numerical model. The results show that the shape of the gas exhaust affects the movement of the vortex core in the gas cyclone. With a change in the shape of the exhaust gas, the axial and tangential velocities changed in the cyclone. The highest turbulent kinetic energy in cyclones was found in the gas exhaust region. The results showed that the diamond gas exhaust exhibited the highest turbulent kinetic energy among the other shapes. In the cases of diamond and square gas exhausts, the size of the Rankine vortex was decreased, leading to a reduction in the centrifugal force of the gas flow and, thereby, cyclone separation efficiency. The lowest erosion rate and highest separation efficiency were found for the cyclone with a circular gas exhaust.

Keywords: Gas Cyclone, Gas Exhaust Shape, Erosion Rate, CFD Simulation

INTRODUCTION

The centrifugal force created by the rotational gas flow motion significantly influences the particle separation performance of cyclones. In a gas cyclone, airflow, including particles, enters from the inlet channel at the cyclone's upper part and generates high rotational velocity in the body of the cyclone. As a result, the larger and denser particles are directed toward the cyclone wall, while the smaller and lighter particles leave the cyclone through the central gas exhaust. Therefore, there is interest in designing cyclone structures with the lowest cost and highest performance. Accordingly, many researchers have studied the influence of geometrical factors on cyclone performance. A brief review of recent related works is presented in this section.

Chuah et al. [1] investigated the impact of changes in the dimensions of the conical section on the flow pattern and performance of gas cyclones. They concluded that increasing the axial and tangential velocities led to an increase in both cyclone performance and pressure drop. Safikhani et al. [2] studied the impact of the number of inlet channels on a new gas cyclone performance using computational fluid dynamics (CFD) tools. Increasing the number of inlet channels increased the cyclone pressure drop and decreased the cyclone efficiency. Qian and Yanpeng [3] studied the effect of inlet channel angle on a gas cyclone by numerical and experimental approaches. They showed that when the inlet channel angle increases, the pressure drop and the collection efficiency increase.

Chen et al. [4] compared one and two-stage gas cyclones using a CFD model. They indicated that the pressure drop in a two-stage gas cyclone is lower than that of a one-stage one. Also, the two-stage gas cyclone showed a better collection efficiency than the one-stage gas cyclone. Cui et al. [5] studied the influence of radial-inlet in gas cyclones used in opposed multi-burner gasification systems. The results indicated that an increase in the particle size causes a rise in collection efficiency. In addition, with the installation of the radial inlet in gas cyclones, the cut-size diameter is reduced compared to that of the conventional gas cyclone under the same condition.

Bogodage and Leung [6] examined the effect of different dust outlet geometries, with and without diplegs at the cyclone bottom, on the flow characteristics and the cyclone performance. It was shown that the dust outlet with a dipleg increases the cyclone efficiency. Safikhani and Mehrabian [7] examined the impact of the length and diameter of vortex limiters using the CFD tool. They showed that the pressure drop decreases as the vortex limiter length

†To whom correspondence should be addressed.
E-mail: s.h.hosseini@ilam.ac.ir

and diameter increase. The influence of the vortex limiter's position and the metal rod's insertion on the heat transfer, performance, and flow pattern of gas cyclones were examined by Yohana et al. [8]. Their results suggested that using the metal rod inside the cyclone improves its efficiency by 13% and the heat rate by 22%.

A brief review regarding the effect of gas exhaust design on cyclone separator efficiency is given here. Parvaz et al. [9] used a CFD model to examine the effect of gas exhaust eccentricity on the flow condition in a gas cyclone. They showed that the eccentricity of the gas exhaust leads to asymmetric flow inside the cyclone and a decrease in the pressure drop. Gao et al. [10] assessed the effects of the gas exhaust diameter and length on the performance of gas-oil cyclones. They found that when the gas exhaust diameter is decreased, the pressure drop and the maximum tangential velocity increase. However, increasing the gas exhaust length has an insignificant influence on the maximum tangential velocity. Lim et al. [11] compared the collection efficiency of cyclones with cylindrical and conical gas exhausts for different flow rates. Their results suggested that the collection efficiencies of two cone-shaped gas exhausts with different diameters are between those of cylindrical gas exhausts with the same diameters. Although the cone-shaped design showed a smaller pressure drop, the cone length did not affect the cyclone's collection efficiency and pressure drop.

Kepa [12] used numerical simulations to analyze the flow and performance of cyclones with double gas exhaust and noticed insignificant effects on collection efficiency. Chen and Liu [13] examined the changes in the gas exhaust geometry on the performance of a cyclone. They showed that the orientation of the gas exhaust slope significantly affects the cyclone pressure drop and efficiency. Tan et al. [14] performed an experimental study of a cylindrical cyclone with no conical bottom and showed that the natural vortex length and collection efficiency decrease with the length and diameter of the gas exhaust. Fu et al. [15] studied the effect of a gas exhaust with side slots in a large gas cyclone. They showed that the slots at the gas exhaust side wall cause a decrease in pressure drop and an increase in collection efficiency. Pei et al. [16] examined the effect of the cylindrical gas exhaust with installed blades on the cyclone separator performance. They showed that the bladed gas exhaust led to a considerable increase in pressure drop and a slight increase in separation efficiency.

Wu and Chen [17] evaluated the shape of gas exhaust internal section effect on cyclone performance. They reported that the cylindrical gas exhaust showed the highest cyclone pressure drop and separation efficiency. El-Batsh [18] studied how the length and diameter of the gas exhaust affect flow pattern and gas cyclone performance. They showed that increasing the diameter of gas exhaust decreases the pressure drop and cyclone performance. However, the gas exhaust length has a negligible effect on cyclone performance.

For square cyclones, Su et al. [19] studied the impact of circular, square, and diamond types of gas exhaust on the performance of the square cyclones using the CFD simulations. Their findings revealed that the separation efficiency increases and the pressure drop decreases for the square gas exhaust compared to the other two. Wasilewski et al. [20] analyzed the influence of the length and diameter of the gas exhaust on the performance of the square cyclones using particle image velocimetry (PIV) and Large eddy simulation (LES). It was found that an increase in the diameter of the gas exhaust caused a considerable increase in the dimensionless pressure drop (Euler number). In contrast, the effect of the gas exhaust length on the Euler number was insignificant. However, the diameter of the gas exhaust affects the separation efficiency for a given gas exhaust length. Finally, Fatahian et al. [21] studied the performance of a square cyclone by analyzing the entrance section geometry of the gas exhaust. They found that although a convergent gas exhaust increases the pressure drop, it allows better separation of finer particles.

Several CFD studies on erosion rates in elbows, pipelines, and cyclones were reported in the literature. Wee and Yap [22], who studied pipeline erosion rates using CFD technique, found that increasing the particle size increases the pipeline's erosion rate. Farokhipour et al. [23] studied the erosion rate of sand particles in pipe bends and reported that the bend erosion rate increases when the particle flow rate increases. Farokhipour et al. [24] investigated the erosion rate in the plugged tees by the CFD-DEM (Discrete Element Method) approach. Their results showed that plugged tees have lower erosion rates than standard elbows. Sedrez et al. [25] performed experimental and CFD studies of the erosion rates in different parts of cyclone walls. They suggested that the Oka and Det Norske Veritas (DNV) erosion models could determine the erosion rates of the cyclone cone and cylindrical sections. Finally, Parvaz et al. [26] studied the effect of the inner cone placed at the bottom of a gas cyclone on the erosion rate and cyclone performance using CFD simulations. They found that the erosion rate decreases with an increase in the restitution coefficient.

More recently, Foroozesh et al. [27] studied the effect of surface roughness on gas cyclone erosion. They found that surface roughness considerably affects the cyclone's airflow behavior and the cyclone wall wear rate. Recently, Dehdarinejad and Bayareh [28] used CFD simulation to examine the impact of non-uniform wall roughness

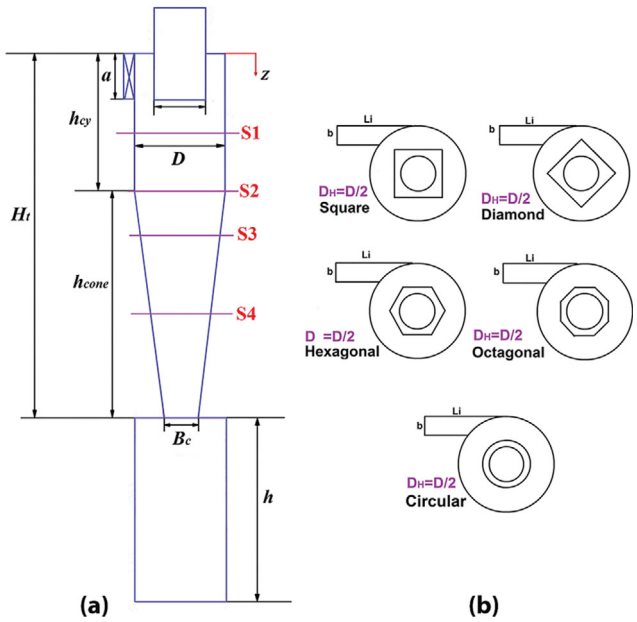

Fig. 1. The cyclone structure (a), with five different gas exhausts (b).

on cyclone performance and erosion. They found that compared to smooth-walled cyclones, cyclones with non-uniform rough surfaces led to higher efficiency for finer particle separation and caused less erosion rate. Finally, Dehdarinejad and Bayareh [29] studied the effect of spiral guide vanes with different pitch lengths on gas cyclone performance using CFD technique. They found that the length and number of guide vanes affect the cyclone performance and erosion rate.

The literature survey shows that the influences of the geometry of gas exhaust cross-section on a conventional circular gas cyclone's performance have not been reported in the past. Therefore, the effect of the exhaust pipe shape on cyclone behavior was evaluated

Table 1. Geometrical dimensions of the gas-solid cyclone studied

Dimension/D	Dimension
Height of inlet, a	a/D=0.5
Width of inlet, b	b/D=0.2
Length of inlet, L_i	L_i/D=1
Diameter of gas outlet, D_H	D_H/D=0.5
Diameter of cone-tip, B_c	B_c/D=0.37
Height of cylindrical part of cyclone, h_{cy}	h_{cy}/D=1.5
Height of cyclone, H_t	H_t/D=4
Height of dustbin, h_d	h_d/D=2

Cyclone body diameter, D=290 mm and D_x is gas exhaust diameter

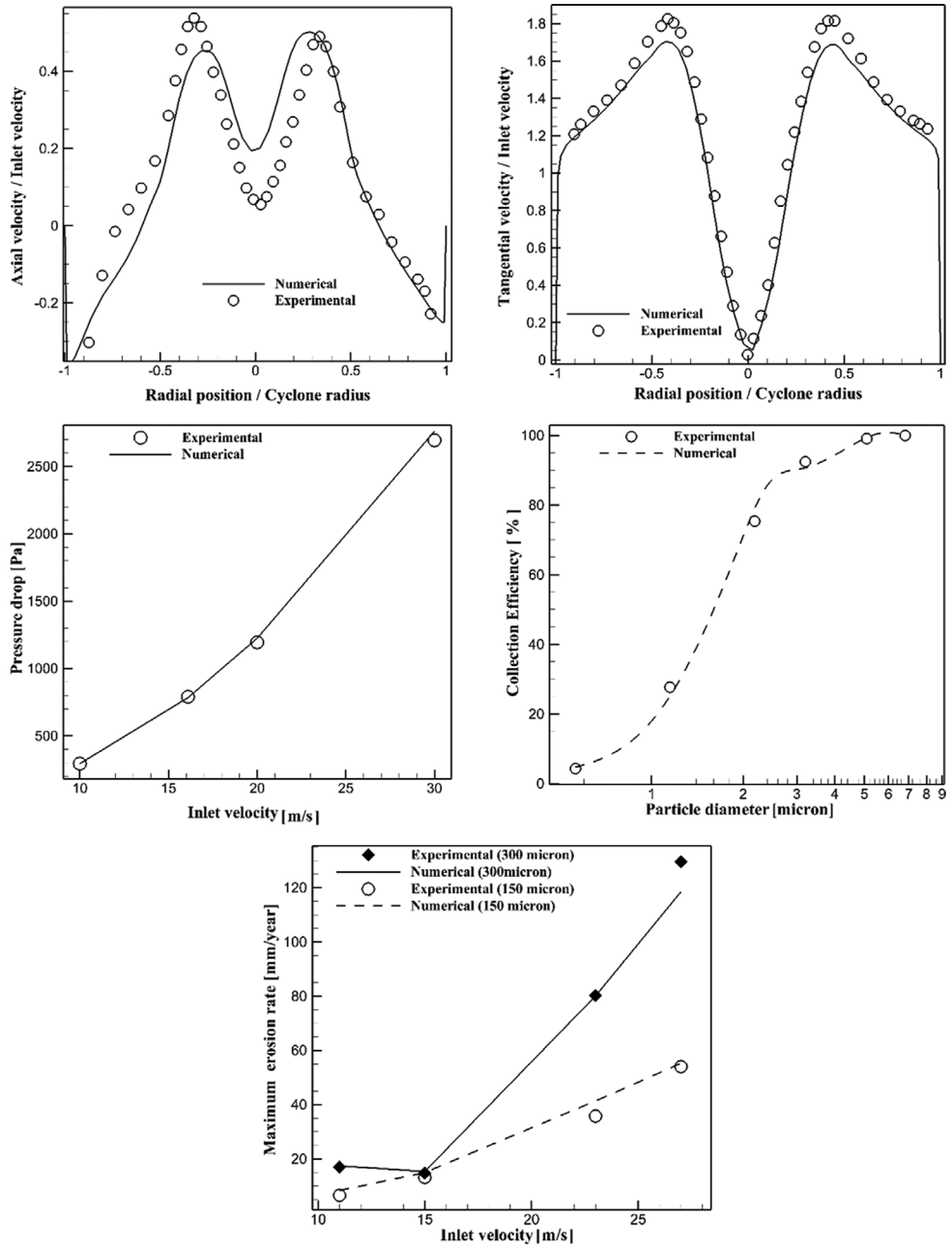

Fig. 2. A comparison of the measured data of axial velocity [31], tangential velocity [31], pressure drop [31], efficiency [32], and erosion rate [33] with the CFD results.

using a computational modeling approach in the present study. Furthermore, the effect of gas exhausts on cyclone erosion rate was examined as another performance factor. The results showed that the gas exhaust shape affected the cyclone's tangential velocity and separation efficiency. The circular gas exhaust, however, was optimal for conventional circular cyclones and showed the lowest erosion rate. Cyclones with circular gas exhausts experience wall erosion mainly on their conical sections. However, cyclones with square and diamond gas exhausts experience wall erosion, mainly on the upper section of the gas cyclone.

CFD MODEL

The governing equations of gas and particle phases and the erosion model, grid sensitivity study results, the boundary conditions, and the solver settings are presented in the Supplementary Materials for brevity. A computational grid with 284,515 cells was chosen for all simulations. Selecting a suitable turbulence model is essential for accurately simulating airflow in gas cyclones [30]. In the present study, the Reynolds stress model (RSM) for turbulence was used for the airflow simulation in all cases. The geometry of the gas exhaust studied is shown in Fig. 1.

The cyclone's dimensions, also depicted in Fig. 1, are listed in Table 1. It should be emphasized that these different exhaust pipes have the same hydraulic diameter. The influence of the selected gas exhaust shapes shown in Fig. 1 on the gas cyclone performance was studied and discussed.

RESULTS AND DISCUSSION

Based on the data of the gas cyclone operated by Hoekstra [31] at inlet velocity of U=16.1 m/s, tangential and axial velocities were predicted at Z/D=0.75 section. In addition, the static pressure drop in the cyclone was compared. Furthermore, the cyclone efficiency was studied and compared with the earlier measured data of Zhao [32]. Finally, the elbow studied by Vieira et al. [33] was simulated to verify the erosion rate prediction. Fig. 2 compares the model results and the corresponding measured data. From Fig. 2, the present model could accurately predict erosion rate, collection efficiency, and cyclone pressure drops under various operating conditions. In addition, the proposed model precisely predicted the axial and tangential gas velocities for V=16.1 m/s at z=0.75D.

1. Axial Velocity

The axial velocity profiles at four levels of S_1, S_2, S_3, and S_4 are presented in Fig. 1 for different gas exhaust shapes to provide information on the flow behavior of various gas cyclones. The dimen-

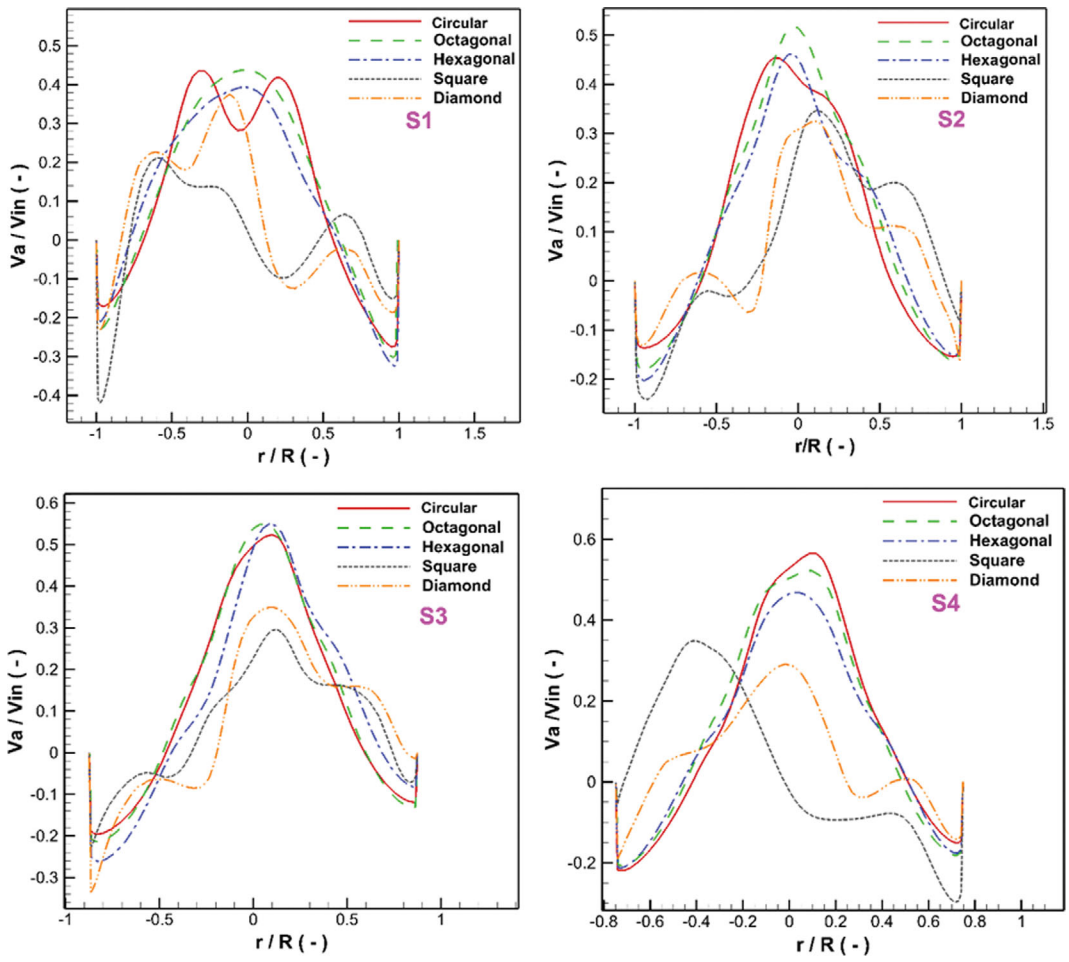

Fig. 3. Axial velocity profiles versus radial distance at different sections for an inlet velocity of V=16.1 m/s.

sionless levels of S_1, S_2, S_3, and S_4 are at Z/D=1, 1.5, 2, and 2.5, respectively, from the top of the cyclone. Note that the motion of the solid particles toward the top of the gas cyclone is mainly controlled by the axial velocity.

Fig. 3 shows the axial velocity profiles for various gas exhaust configurations on levels S_1, S_2, S_3, and S_4. In conventional gas cyclones, the axial velocity is composed of upward and downward components. Near the wall, the airflow has a downward direction, while near the cyclone center, the flow is in a positive direction (upward). The cyclones with circular, hexagonal, and octagonal gas exhausts display similar qualitative behavior. Examining the axial velocity profiles in sections S_1, S_2, S_3, and S_4 shows that the gas exhaust's geometry profoundly affects the flow field. Furthermore, among the different gas exhausts, the square and diamond geometries show the most complex and almost irregular behavior of axial velocity profiles at various cyclone levels, particularly in the cyclone core region. It is found that with increasing the number of sides in the gas exhaust cross-section geometry, the flow behavior remains similar. The inverse W-shaped velocity profile only occurs for the cyclone with circular gas exhaust. For circular gas exhausts, the inverse W-shaped velocity profiles change to an inverse V-shaped profile at the bottom, weakening vortex core retention. However, the hexagonal and octagonal gas exhausts display V-shaped velocity profiles at different cyclone levels. The cyclone with square gas exhaust has the minimum axial velocity. The cyclones with square and diamond gas exhausts show wavy axial velocity profiles. Note that there is resistance to flow exiting the cyclone through square and diamond gas exhausts, resulting in wavy vortexes and asymmetric and non-uniform axial velocity profiles. In contrast, the cyclones with circular, hexagonal, and octagonal outlets exhibit the highest axial velocity compared with those of square and diamond geometries.

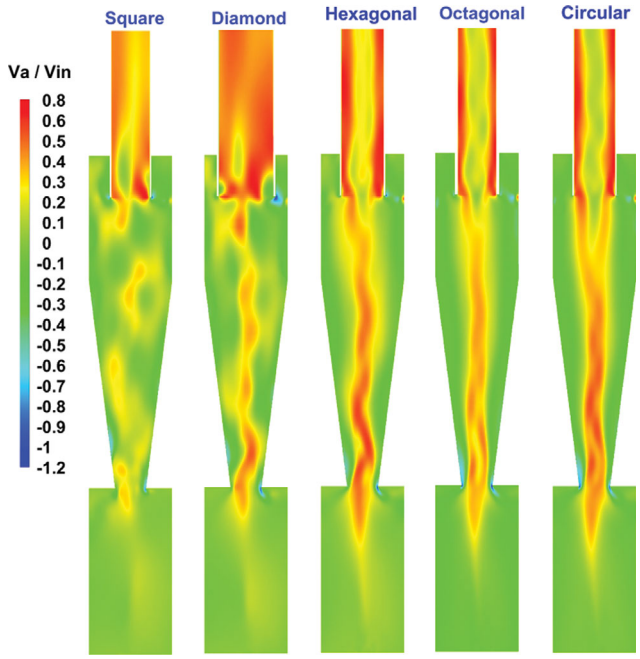

Fig. 4. Axial velocity contours on the X-Z (Y=0) plane of cyclones with different gas exhausts for V=16.1 m/s.

Fig. 4 illustrates the axial velocity contour plots at the mid-plane of cyclones with different gas exhaust geometries. This figure shows that the maximum axial velocity appears in the gas exhaust region in all cases. Although the axial velocity increases towards the gas exhaust wall from the core region in the cases of circular, hexagonal, and octagonal gas exhausts, the distributions of airflow in the diamond and square gas exhausts do not follow the same trend, which affects gas cyclone performance.

According to Fig. 4, the greatest axial velocity is seen in the central axis of the cyclone when the gas exhausts are circular, hexagonal, or octagonal. However, deviations are seen when the gas exhaust is diamond or square.

2. Tangential Velocity

The tangential airflow velocity in a gas cyclone is a critical factor that significantly affects the efficiency of solid particle separation and the cyclone pressure drop. The tangential velocity produces the centrifugal force, which pushes particles toward the cyclone wall and separates them from the gas flow. The tangential velocity mainly consists of forced and free vortices. Fig. 5 exhibits the profiles of dimensionless tangential velocity at various sections S_1, S_2, S_3, and S_4 in the cyclones with different gas exhaust geometries for the inlet velocity of 16.1 m/s. For the circular, hexagonal, and octagonal gas exhausts, a gradual increase in the tangential velocity is observed away from the central axis up to its maximum value, decreasing towards the wall. In addition, the trends of tangential velocity at different levels of the cyclones with circular, hexagonal, and octagonal gas exhausts are the same.

As mentioned, when the number of sides of gas exhaust cross-section geometry increases, the flow behaves more like that observed in the cyclone with a circular gas exhaust. Accordingly, similar trends are expected in cyclones with circular, octagonal, and hexagonal gas exhausts. In contrast, tangential velocity profiles are distorted for the diamond and square gas exhausts. Moreover, the diamond and square gas exhausts show asymmetrical behavior due to the effect of their corners. Therefore, based on Figs. 3 and 5, it is concluded that the tangential and axial gas velocity profiles in the cyclone are markedly affected by the gas exhaust geometry. In addition, the Rankine vortex size in the cyclone with circular, octagonal, and hexagonal gas exhausts is smaller than those with the diamond and square gas exhausts. Finally, as seen in Fig. 5, the maximum tangential gas velocity occurs for circular gas exhaust geometry, which means that the circular shape enhances cyclone separation efficiency.

Fig. 6 shows the contour of tangential velocity on the mid-plane of cyclones with various gas exhausts. It is seen that the tangential velocity forms a strong free vortex flow in cyclones with circular, octagonal, and hexagonal gas exhausts. For cyclones with square and diamond gas exhausts, however, the free vortex is distorted, and the tangential velocity in the core becomes negative due to the strong flow asymmetry. As noted, for hexagonal, octagonal, and circular gas exhausts, the tangential velocity increases and shows a symmetry behavior in the gas cyclone.

3. Turbulence Kinetic Energy

The turbulent kinetic energy (TKE) is the sum of mean-square velocity fluctuations and is an important measure of turbulence

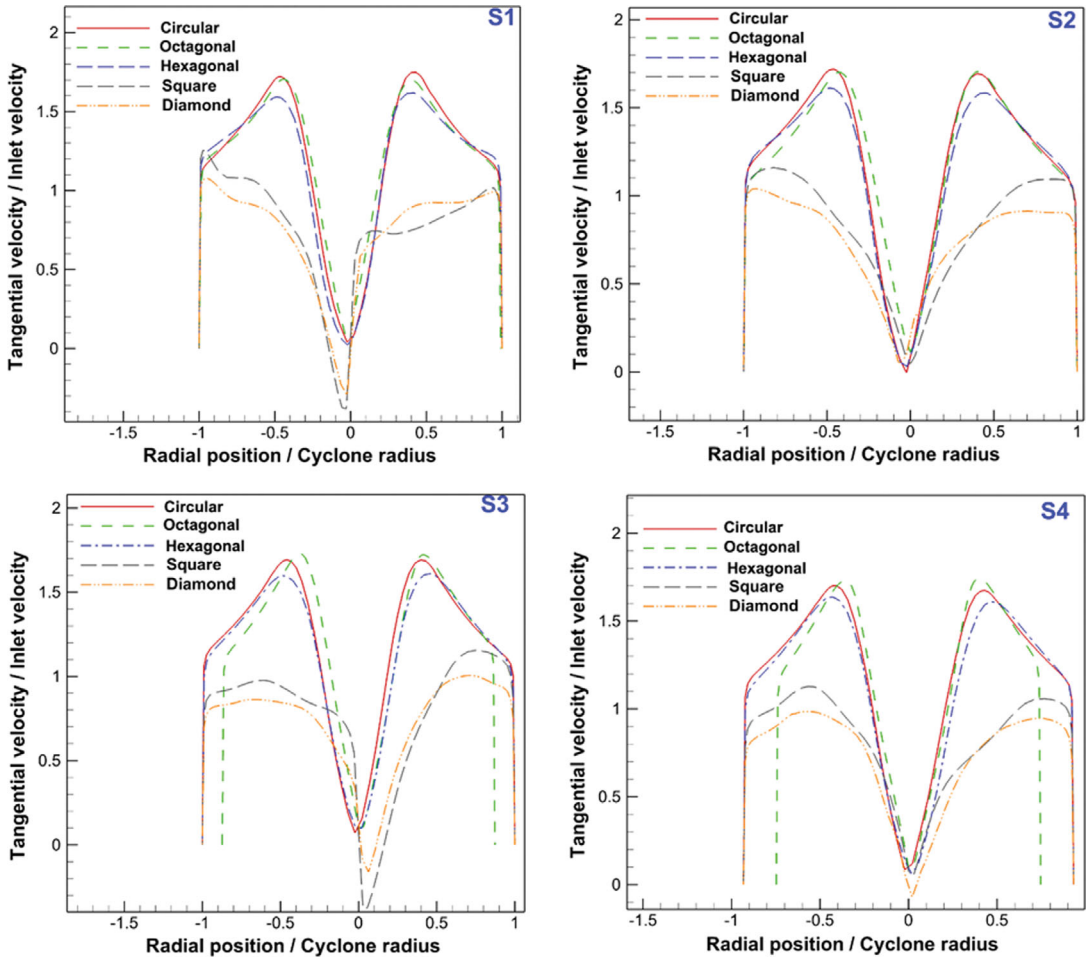

Fig. 5. The tangential velocity profiles versus radial distance at different sections for an inlet velocity of V=16.1 m/s.

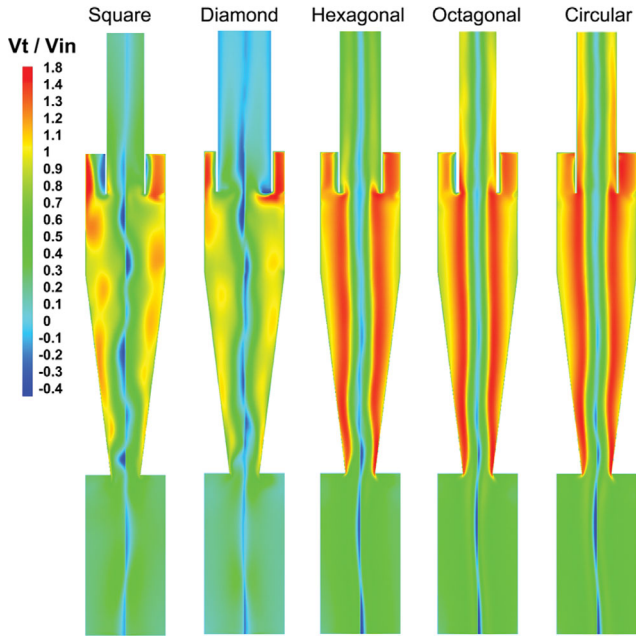

Fig. 6. Tangential velocity contours on the X-Z plane (Y=0) in cyclones with different gas exhausts for V=16.1 m/s.

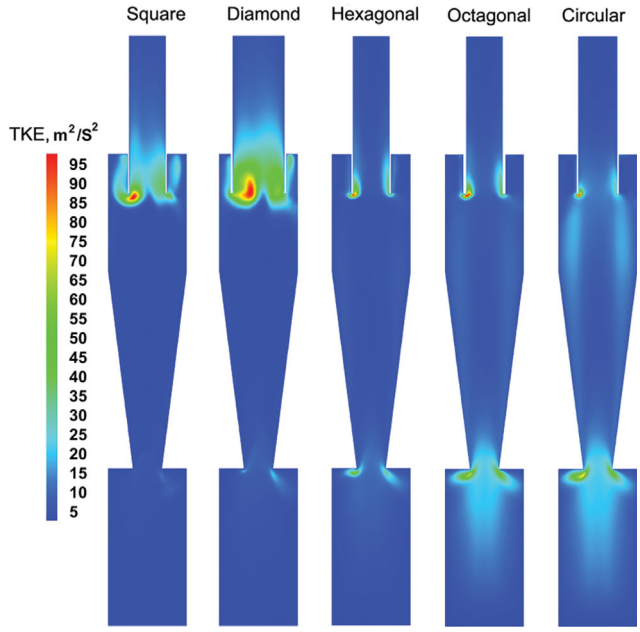

Fig. 7. Turbulence kinetic energy contours at the mid-section of gas cyclones with different gas exhausts for an inlet airflow velocity of V=16.1 m/s.

intensity in the flow field. The TKE affects the dispersion of particles as they are transported by airflow. Fig. 7 exhibits the contour plots of turbulence kinetic energy distribution in the gas cyclones equipped with different gas exhausts. It is seen that the gas outlet shape affects the magnitude of the turbulence kinetic energy in the gas cyclone. Similar to the previous studies [16,19,34-37], for all cases, the maximum TKE is found in the gas exhaust inlet, near the pipe wall, due to the presence of local vortices in this region. In addition, a slight change in TKE occurs in the main cyclone body. The separation efficiency decreases with an increase of TKE in the gas exhaust. The main cause is that most particles are separated in the outer vortex due to the high airflow tangential velocity [16]. Note that in the cyclone with circular gas exhaust, except for the entrance of gas exhaust, the TKE value is slightly higher than the other exhaust pipe shapes.

Furthermore, an increase in the TKE in the center of the gas outlet decreases particle trapping. Fig. 7 also shows that the highest TKE values in dustbins and lower parts of cyclones are found in the cyclone with a circular gas exhaust.

In gas cyclones, the airflow field is closely influenced by vortex behavior, which contributes to the centrifugal force. In addition, the Q criterion, which recognizes the vortex structure, describes the vortex performance in cyclones. Fig. 8 exhibits the three-dimensional iso-vortex surface in the gas cyclones with various gas exhaust geometries based on Q=1,000 s^{-2}. As seen, the cyclones with circular, octagonal, and hexagonal gas exhausts show the smooth circular surface of the vortex core. However, the cyclones with square and diamond gas exhausts cause some irregularities in the vortex structure along the central axis due to their corners, especially at the top, where TKE is highest. Furthermore, vortex stability is achieved using circular, octagonal, and hexagonal gas exhausts.

4. Pressure Drop

Generally, vortical airflow motion is attributed to the radial pressure drop distribution in the body of the cyclone. The static pressure contour plots at the mid-plane of the cyclones with different gas exhausts for an inlet gas velocity of 16.1 m/s are shown in Fig. 9. It is seen that the static pressure distributions in the cyclones are similar for the circular, octagonal, and hexagonal gas exhausts. However, the static pressure distribution in the cyclones with square and diamond exit tubes is entirely different from that of the other cyclones. Fig. 9 also shows that the gas exhaust shape significantly affects the gas cyclones' hydrodynamic parameters and static pressure variation.

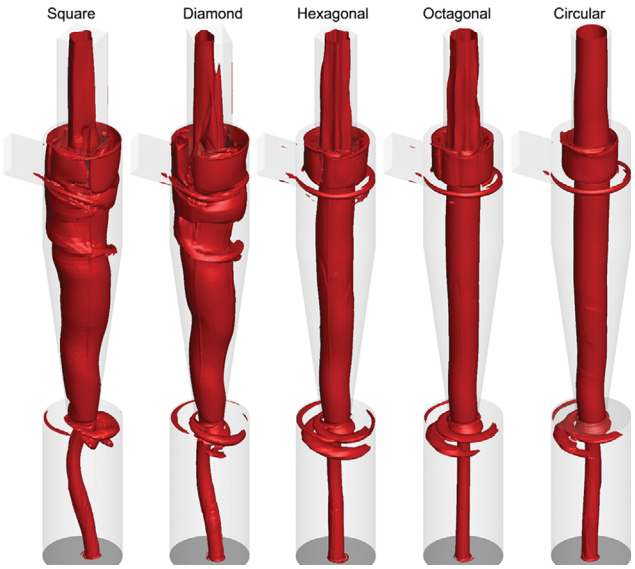

Fig. 8. 3D iso-vortex surface of the cyclones with different gas exhausts for an inlet airflow velocity of V=16.1 m/s.

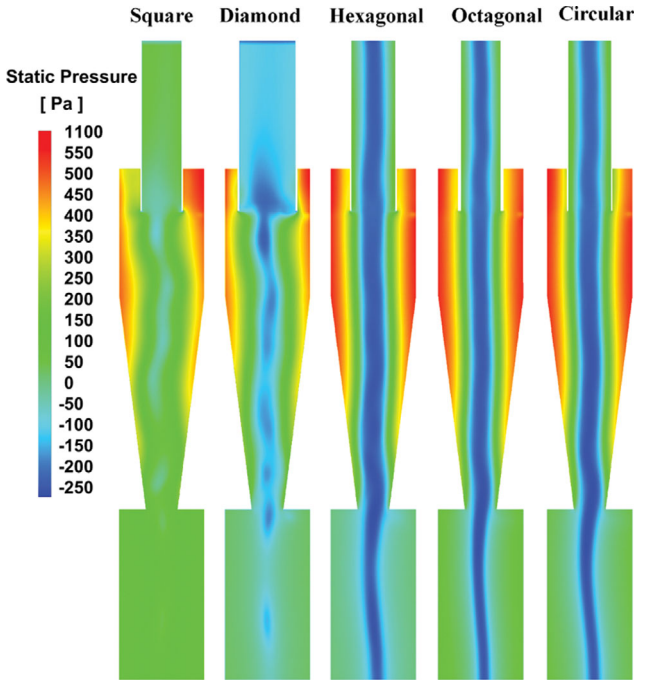

Fig. 9. Static pressure contours at the mid-section of gas cyclones with different gas exhausts for an inlet airflow velocity of V=16.1 m/s.

The value of static pressure is important in cyclones, and its main variations are in three areas: (1) at inlets, (2) in cyclone walls of the main body, and (3) at gas exhausts. As reported in [38], the radial pressure gradient is proportional to the square flow tangential velocity u_t^2. Therefore, the pressure drop in gas cyclones increases as the tangential velocity increases. This trend is also observed in the presented CFD results (Figs. 5 and 10). In addition, static pressure increases from the central part of the cyclone, where axial velocity is highest, to the walls of the cyclone, where velocity is zero, due to an increase in dissipation rate [39-41]. Fig. 10 illustrates radial pressure profiles in sections S_1, S_2, S_3, and S_4. The maximum pressure value is observed on the walls of the cyclones due to the flow resistance, but it is minimum in the central part of the gas cyclones because of the centrifugal force effect. Fig. 10 shows that the radial pressure profiles are greatly affected by the different gas exhaust cross-sections. The cyclones with diamond and octagonal gas exhausts have the lowest and the highest static pressures near the wall, respectively. The cyclones with circular, hexagonal, and octagonal gas exhausts exhibit symmetric static pressure profiles. In contrast, the cyclones with square and diamond gas exhausts exhibit asymmetric static pressure variation due to the non-uniform axial

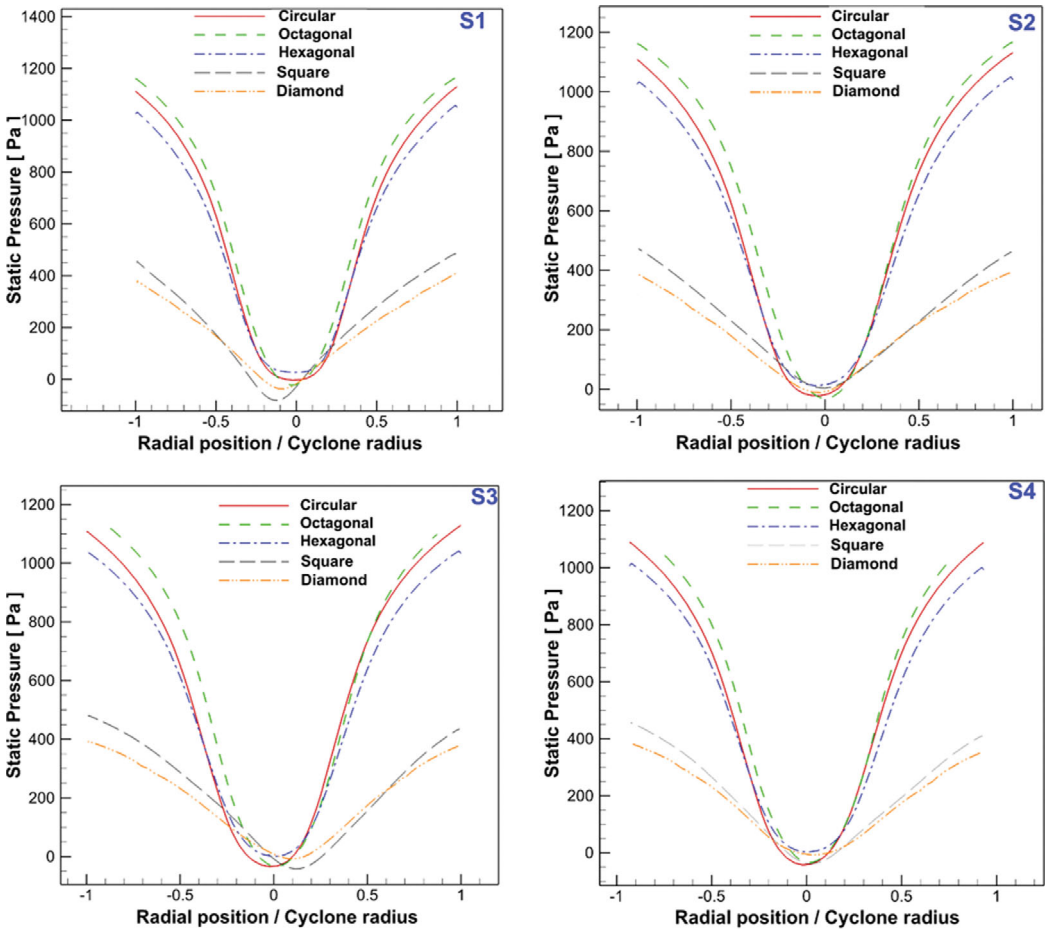

Fig. 10. Variation of the radial static pressure profiles for different gas exhaust shapes for an inlet airflow velocity of V=16.1 m/s.

velocity profiles in the central region of the cyclones. As stated, the static pressure profiles for the circular, octagonal, and hexagonal gas exhausts are roughly the same, while the square and diamond gas exhausts show much lower static pressure values.

5. Separation Efficiency

In gas cyclones, separation efficiency is defined as,

$$\eta=\left(1-\frac{n_{out}}{n_{total}}\right)\times 100(\%) \quad (1)$$

where n_{out} stands for the number of particles that escape from the exit tube with the gas flow, and n_{total} for the total number of solid particles that entered the cyclone separator. The effect of the gas exhaust shape on the cyclone's separation performance is of critical interest. Fig. 11 compares the separation efficiencies of the cyclones with various gas outlet shapes for U=16.1 m/s. As expected, the separation efficiency gradually increases with the particle size. The capture efficiencies for cyclones with cylindrical, octagonal, and hexagonal gas exhausts show the S-shaped profiles. However, the square and diamond exit tubes lead to monotonically increasing separation efficiencies with particle size. The cyclone with a circular gas exhaust has the highest separation efficiency due to the highest tangential velocity at different cyclone levels.

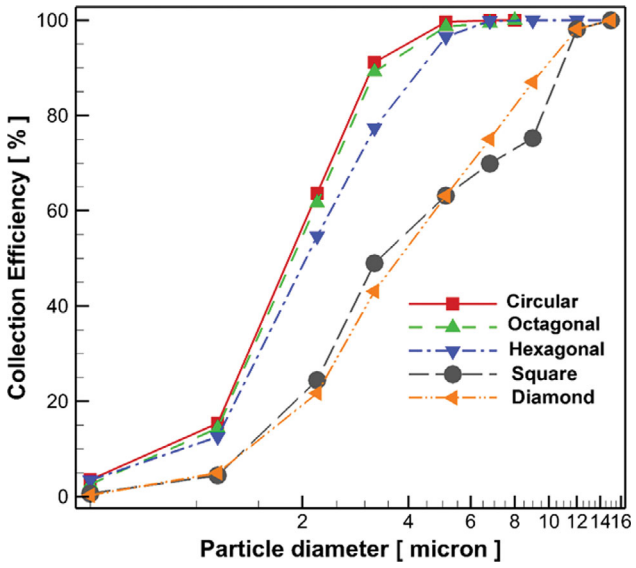

Fig. 11. The cyclone separation efficiency for different gas outlet shapes.

6. Erosion Rate

The model validation showed that the Oka model accurately predicts the erosion rate for the 150 and 300 μm particles in 90-degree elbows. Therefore, the Oka model was used to study the

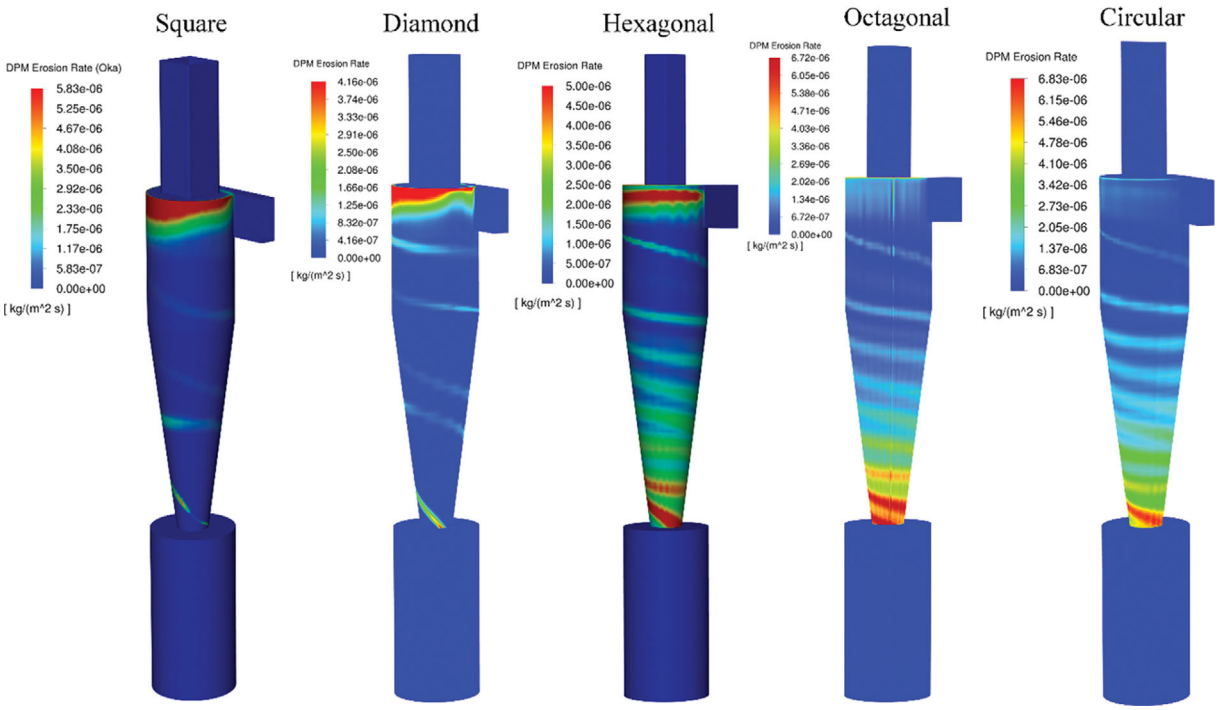

Fig. 12. Contour plots of erosion rates for different gas exhaust shapes for an inlet airflow velocity of 16.1 m/s.

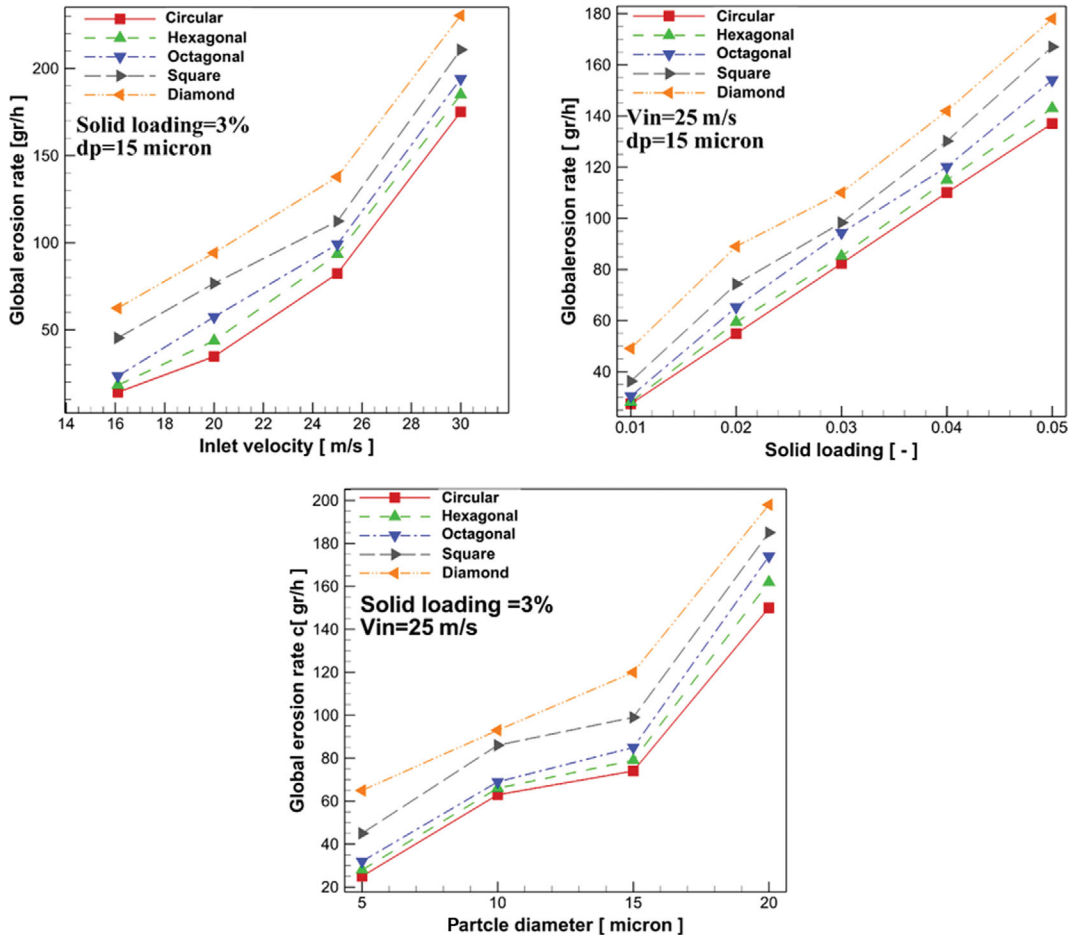

Fig. 13. Variations of cyclone erosion rates for different inlet velocities, solid loadings, and particle sizes.

erosion rate for gas cyclones with different gas exhausts operating for various inlet velocities and particle sizes. Fig. 12 displays the contour plots of erosion rate on the circular and conical parts for cyclones with different exit pipes for U=16.1 m/s and solid loading of 5%. It is seen that gas exhaust geometry significantly affects the cyclone erosion rate. Flow patterns, including tangential velocity, radial velocity, and vortex stability, affect the impact of solid particles on the wall and the corresponding erosion rates.

According to Fig. 12, the maximum erosion rate occurs on the upper part of the cylindrical section of the cyclone with the square, diamond, and hexagonal gas exhausts due to high gas velocity in these regions. However, the cyclones with circular and octagonal gas exhausts show less erosion rate in this area. In cyclones with circular and octagonal exit pipes, the maximum erosion rate is observed in the conical section of the gas cyclone. Earlier studies concerning erosion rate in cyclones with circular gas exhaust showed similar results [26-28,42].

Fig. 13 shows the variation of the cyclone erosion rates with different gas exhausts for various inlet velocities, solid loadings, and particle sizes. It is observed that the cyclones with different gas exhausts are eroded differently by solid loading, particle size, and inlet velocity. That is, in addition to the noted parameters, the cyclone erosion rate is affected by the gas exhaust shape. Fig. 13 shows that the erosion rate increases when the inlet velocity, solid loading, and particle size increase. In addition, the gas exhaust shape significantly affects the cyclone erosion rate. The maximum and minimum erosion rates occur for diamond-shaped and circular gas exhaust geometries, respectively.

Static pressure rising at the cyclone walls increases erosion rates, as reported in previous work [27]. However, the diamond gas exhaust offers the lowest pressure drop but exhibits the highest erosion rate on the cyclone walls, especially near the gas inlet. Therefore, the static pressure does not control erosion alone. This area needs further investigation.

CONCLUSIONS

The present work studied airflows in a conventional gas cyclone with different gas exhausts using a validated CFD model. The RSM turbulence model was used for the airflow simulation in all cases. In addition, the DPM was used to simulate the solid particle motions to evaluate the collection efficiency and erosion rate. The main conclusions are as follows:

1) The gas exhaust shape affects the cyclone's tangential and axial gas velocities, static pressure, and separation efficiency.
2) Using a diamond-shaped gas exhaust showed the lowest static pressure and tangential velocity among the other shapes.
3) The circular gas exhaust showed the highest separation efficiency compared to the other geometries.
4) The cyclone with a circular cylinder gas exhaust showed the lowest erosion rate among the cases studied.
5) Cyclones with square and diamond gas exhausts experience wall erosion, mainly on the upper section of the gas cyclone. In contrast, cyclones with circular, hexagonal, and octagonal gas exhausts experience wall erosion mainly on their conical sections.

SUPPORTING INFORMATION

Additional information as noted in the text. This information is available via the Internet at http://www.springer.com/chemistry/journal/11814.

REFERENCES

1. T. G. Chuah, J. Gimbun and T. S. Y. Choong, *Powder Technol.*, **162**, 126 (2006).
2. H. Safikhani, J. Zamani and M. Musa, *Adv. Powder Technol.*, **29**, 611 (2018).
3. F. Qian and Y. Wu, *Chem. Eng. Res. Des.*, **87**, 1567 (2009).
4. J. Chen, B. Yang, Z. A. Jiang and Y. Wang, *ACS Omega*, **4**, 13603 (2019).
5. J. Cui, X. Chen, X. Gong and G. Yu, *Ind. Eng. Chem. Res.*, **49**, 5450 (2010).
6. S. Ganegama Bogodage and A. Y. T. Leung, *Powder Technol.*, **286**, 488 (2015).
7. H. Safikhani and P. Mehrabian, *Adv. Powder Technol.*, **27**, 379 (2016).
8. E. Yohana, M. Tauviqirrahman, B. Yusuf, K. H. Choi and V. Paramita, *Powder Technol.*, **377**, 464 (2021).
9. F. Parvaz, S. H. Hosseini, G. Ahmadi and K. Elsayed, *Sep. Purif. Technol.*, **187**, 1 (2017).
10. X. Gao, J. Chen, J. Feng and X. Peng, *Comput. Fluids*, **92**, 45 (2014).
11. K. S. Lim, H. S. Kim and K. W. Lee, *J. Aerosol Sci.*, **35**, 743 (2004).
12. A. Kçpa, *Sep. Purif. Technol.*, **75**, 127 (2010).
13. J. Chen and X. Liu, *Sep. Purif. Technol.*, **73**, 100 (2010).
14. F. Tan, I. Karagoz and A. Avci, *Chem. Eng. Commun.*, **203**, 1216 (2016).
15. S. Fu, F. Zhou, G. Sun, H. Yuan and J. Zhu, *Adv. Powder Technol.*, **32**, 931 (2021).
16. B. Pei, L. Yang, K. Dong, Y. Jiang, X. Du and B. Wang, *Powder Technol.*, **313**, 135 (2017).
17. X. Wu and X. Chen, *Environ. Prog. Sustain. Energy*, **38**, 1 (2019).
18. H. M. El-Batsh, *Appl. Math. Model.*, **37**, 5286 (2013).
19. Y. Su, B. Zhao and A. Zheng, *Ind. Eng. Chem. Res.*, **50**, 12162 (2011).
20. M. Wasilewski, L. S. Brar and G. Ligus, *Sep. Purif. Technol.*, **239**, 10 (2020).
21. E. Fatahian, H. Fatahian, E. Hosseini and G. Ahmadi, *Powder Technol.*, **387**, 454 (2021).
22. S. K. Wee and Y. J. Yap, *J. Pet. Sci. Eng.*, **176**, 269 (2019).
23. A. Farokhipour, Z. Mansoori, M. Saffar-Avval and G. Ahmadi, *Sci. Iran*, **25**, 3231 (2018).
24. A. Farokhipour, Z. Mansoori, A. Rasteh, M. A. Rasoulian, M. Saffar-Avval and G. Ahmadi, *Powder Technol.*, **352**, 136 (2019).
25. T. A. Sedrez, R. K. Decker, M. K. da Silva, D. Noriler and H. F. Meier, *Powder Technol.*, **311**, 120 (2017).
26. F. Parvaz, S. H. Hosseini, K. Elsayed and G. Ahmadi, *Sep. Purif. Technol.*, **201**, 223 (2018).
27. J. Foroozesh, F. Parvaz, S. H. Hosseini, G. Ahmadi, K. Elsayed and N. U. Babaoğlu, *Powder Technol.*, **389**, 339 (2021).
28. E. Dehdarinejad and M. Bayareh, *Chem. Eng. Sci.*, **249**, 117351 (2022).
29. E. Dehdarinejad and M. Bayareh, *J. Brazilian Soc. Mech. Sci. Eng.*,

44, 516 (2022).
30. E. Dehdarinejad and M. Bayareh, *ChemBioEng Rev.*, **8**, 375 (2021).
31. A. J. Hoekstra, *Gas flow field and collection efficiency of cyclone separators* (2000).
32. B. Zhao, *Chem. Eng. Process. Process Intensif.*, **44**, 447 (2005).
33. R. E. Vieira, A. Mansouri, B. S. McLaury and S. A. Shirazi, *Powder Technol.*, **288**, 339 (2016).
34. S. Wang, H. Li, R. Wang, X. Wang, R. Tian and Q. Sun, *Adv. Powder Technol.*, **30**, 227 (2019).
35. J. Duan, S. Gao, C. Hou, W. Wang, P. Zhang and C. Li, *Powder Technol.*, **372**, 305 (2020).
36. O. Hamdy, M. A. Bassily, H. M. El-Batsh and T. A. Mekhail, *Appl. Math. Model.*, **46**, 81 (2017).
37. Y. Su, A. Zheng and B. Zhao, *Powder Technol.*, **210**, 293 (2011).
38. C. Cortés and A. Gil, *Prog. Energy Combust. Sci.*, **33**, 409 (2007).
39. S. Ganegama Bogodage and A. Y. T. Leung, *J. Hazard. Mater.*, **311**, 100 (2016).
40. L. S. Brar and K. Elsayed, *Powder Technol.*, **311**, 465 (2017).
41. J. Gimbun, T. G. Chuah, T. S. Y. Choong and A. Fakhru'l-Razi, *J. Aerosol Sci.*, **36**, 1056 (2005).
42. E. Dehdarinejad, M. Bayareh and M. Ashrafizaadeh, *Chem. Pap.*, **76**, 5579 (2022).

Supporting Information

Influence of gas exhaust geometry on flow pattern, performance, and erosion rate of a gas cyclone

Farzad Parvaz*, Seyyed Hossein Hosseini,†, Ahmad Reza Bastan**, Jamal Foroozesh***, Nihan Uygur Babaoğlu****, Khairy Elsayed*****,******, and Goodarz Ahmadi*******

*Department of Mechanical Engineering, Semnan University, P.O. Box 35131-191, Semnan, Iran
**Department of Chemical Engineering, Ilam University, Ilam 69315-516, Iran
***Department of Metallurgy and Materials Science, Faculty of Engineering, Shahid Bahonar University of Kerman, Kerman, Iran
****Department of Environmental Engineering, Kahramanmaras Sutcu Imam University, Kahramanmaras, Turkey
*****Mechanical Power Engineering Department, Faculty of Engineering at El-Mattaria, Helwan University, Masaken El-Helmia P.O., Cairo 11718, Egypt
******Mechanical Engineering Department, College of Engineering and Technology-Smart Village Campus, Arab Academy for Science, Technology and Maritime Transport (AASTMT), P.O. Box 12676, Giza, Egypt
*******Department of Mechanical and Aerospace Engineering, Clarkson University, Potsdam, NY 13699-5725, USA
(*Received 9 October 2022 • Revised 20 January 2023 • Accepted 13 February 2023*)

1. Governing Equations

1-1. Turbulence Model

In this study, we used the RSM turbulence model to simulate gas flows in cyclones accurately. For an incompressible fluid, the governing equations of continuity and balance of momentum were given as:

$$\frac{\partial \overline{u_i}}{\partial x_i}=0 \tag{1}$$

$$\frac{\partial \overline{u_i}}{\partial t}+\overline{u_j}\frac{\partial \overline{u_i}}{\partial x_j}=-\frac{1}{\rho}\frac{\partial \overline{P}}{\partial x_i}+\nu\frac{\partial^2 \overline{u_i}}{\partial x_i \partial x_j}-\frac{\partial}{x_j}R_{ij} \tag{2}$$

where u_i is the mean velocity, x_i is the position, $\overline{P}$ is the mean pressure, ρ is the gas density, ν is the gas kinematic velocity, and $Rij=\overline{u_i' u_j'}$ denotes the Reynolds stress tensor. Here $u_i'=u_i-\overline{u_i}$ is the i*th* fluctuating velocity component. The RSM turbulence model provides the transport equation for evaluating the turbulence stress components. That is,

$$\frac{\partial}{\partial t}R_{ij}+\overline{u_k}\frac{\partial}{\partial x_k}R_{ij}=\frac{\partial}{\partial x_k}\left(\frac{\nu_t}{\sigma^k}\frac{\partial}{\partial x_k}R_{ij}\right)-\left[R_{ik}\frac{\partial \overline{u_j}}{\partial x_k}+R_{jk}\frac{\partial \overline{u_i}}{\partial x_k}\right]$$
$$-C_1\frac{\varepsilon}{k}\left[R_{ij}-\frac{2}{3}\delta_{ij}K\right]-C_2\left[P_{ij}-\frac{2}{3}\delta_{ij}P\right]-\frac{2}{3}\delta_{ij}\varepsilon \tag{3}$$

where the turbulence production terms P_{ij} is defined as,

$$P_{ij}=-\left[R_{ik}\frac{\partial \overline{u_j}}{\partial x_k}+R_{jk}\frac{\partial \overline{u_i}}{\partial x_k}\right],\ P=\frac{1}{2}P_{ij} \tag{4}$$

Here P denotes the fluctuating kinetic energy production, ν_t stands for the turbulence (eddy) kinematic viscosity, and σ^k=1, C_1=1.8, C_2=0.8 are empirical constants.

The transport equation for the turbulence dissipation rate, ε, can be written as:

$$\frac{\partial \varepsilon}{\partial t}+\overline{u_j}\frac{\partial \varepsilon}{\partial x_j}=\frac{\partial}{\partial x_j}\left[\left(\upsilon+\frac{\upsilon_t}{\sigma^{\varepsilon}}\right)\frac{\partial \varepsilon}{\partial x_j}\right]-C^{\varepsilon 1}\frac{\varepsilon}{K}R_{ij}\frac{\partial \overline{u_i}}{\partial x_j}-C^{\varepsilon 2}\frac{\varepsilon^2}{K} \tag{5}$$

where $K=\frac{1}{2}\overline{u_i' u_j'}$ is the fluctuating kinetic energy. The values of constants are

σ^{ε}=1.3, $\sigma^{\varepsilon 1}$=1.44, $\sigma^{\varepsilon 2}$=1.92

1-2. Particle Motion

In the present study, the Eulerian-Lagrangian method is used. The particle trajectory is determined according to Newton's second law. That is, the equation of motion of a solid particle is as,

$$\frac{d\vec{x}_p}{dt}=\vec{u}_p \tag{6}$$

$$\frac{d\vec{u}_p}{dt}=F_D(\vec{u}-\vec{u}_p)+\vec{a} \tag{7}$$

where the terms in the right of Eq. (7) are the drag force and the gravity/buoyancy acceleration term, which are given as,

$$F_D=\frac{18\mu}{\rho_p d_p^2}\frac{C_D Re}{24} \tag{8}$$

$$\vec{a}=\vec{g}\left(\frac{\rho_p-\rho}{\rho_p}\right) \tag{9}$$

The virtual mass, the Basset force, and the Saffman lift force are also ignored in these equations. The Reynolds number in Eq. (8) is given by,

$$Re=\frac{\rho d_p\left|\vec{u}_p-\vec{u}\right|}{\mu} \tag{10}$$

The empirical correlation proposed by Schiller and Naumann [1]

Table S1. The value of constant in the Oka erosion model

Parameter	ζ	k_1	k_2	k_3	n_1	n_2	H_v (GP)	d' (μm)	V' (m/s)
Value	65	−0.12	2.35	0.19	0.77	1.36	1.83	326	104

is used to evaluate the drag coefficient for a smooth sphere:

$$C_D=\begin{cases}\dfrac{24}{Re_p} & Re_p<0.1\\ \dfrac{24}{Re_p}(1+0.15Re_p^{0.687}) & 0.1<Re_p\le 1{,}000\\ 0.44 & Re_p>1{,}000\end{cases} \quad (11)$$

1-3. Erosion Modeling

The solid particles carried by the flow cause erosion in cyclones, elbows, and pipelines. In gas cyclones, the solid particle collisions with the cyclone walls erode the walls over time. The erosion model of Oka et al. [2,3], broadly used for evaluating erosion rates in various systems, is utilized here. The rate of erosion is determined as,

$$E_R=\sum_{n=1}^{N_p}\frac{E^{(i)}}{A_{face}} \quad (12)$$

where E_R is the removed mass flux (Kg/m^2 s). E_R is integrated over the total area of the gas cyclone. In Eq. (17), the erosion rate, $E^{(i)}$, is calculated by

$$\begin{cases}E^{(i)}=1\times10^{-9}E_V\rho_w\dot{m}_P\\ E_V=f(\alpha)E_{90}\\ E_{90}=\zeta(H_v)^{k_1}\left(\dfrac{V_P^{(i)}}{V'}\right)^{k_2}\left(\dfrac{d_P}{d'}\right)^{k_3}\\ f(a)=(\sin\alpha)^{n_1}[1+H_v(1-\sin\alpha)]^{n_2}\end{cases} \quad (13)$$

where ρ_w=7,990 kg/m^3 is the cyclone wall density, α is the impact angle and $F(\alpha)$ denotes the function of impact angle, H_V is the Vickers hardness of the stainless steel 316 (SS316) of cyclone wall, V' and d' are the standard velocity and standard particle diameter, respectively. In addition, $V_P^{(i)}$ is particle velocity. The value of k_1, k_2, k_3, n_1, n_2 and ζ are listed in Table S1.

2. Grid Study

The creation of the computational grid, covering the entire cyclone gas flow region, is an important step for obtaining accurate CFD results. Fig. S1 shows the computational grids for different cases under study. This figure shows that the hexagonal meshes are used in the computational domains. The grids near the cyclone walls are much denser than the other regions. Here, the mesh independence study was performed for different grids in terms of Euler and Stokes numbers, and the results are presented in Table S2. It is observed that the grids with 284515 and 571429 cells show roughly the same results. Accordingly, the grid with 284515 cells is used in the subsequent simulations to reduce the computational cost.

3. Boundary Condition

In these simulations, the airflow is considered incompressible and isothermal, and the inlet gas velocity is considered uniform. The outlet of the exhaust tube is treated as the outflow boundary condition. In addition, on the cyclone walls, the no-slip velocity condition is used. The air density is 1.225 (kg/m^3), the particle density is 2,750 (kg/m^3), and the air dynamic viscosity is 1.7 e^{-5} (Pa s). The inlet airflow turbulence intensity is 5%, and the characteristic length is 0.07 times the inlet width [4]. The unsteady airflow is simulated with RSM, and the resident time is calculated as,

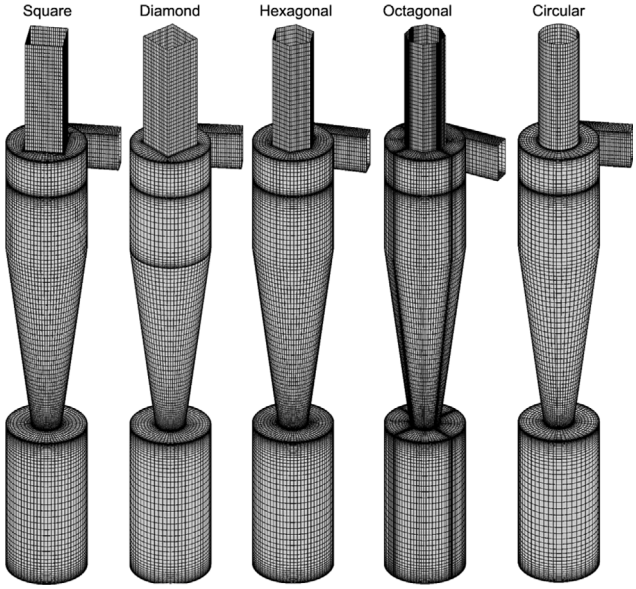

Fig. S1. Computational grids for the gas cyclones with different outlet pipe shapes.

Table S2. The grid independence results

Number of cells	Euler number $\left(\dfrac{2\Delta P}{\rho u_{in}^2}\right)^{1*}$	Stokes number $\left(St_{50}=\dfrac{(\rho_P-\rho_g)x_{cut}^2u_{in}}{18\mu D}\right)^{2*}\times10^{-2}$
197205	5.13	0.06
284515	4.95	0.05
402020	4.91	0.05
571429	4.96	0.05
Different (%)[a]	4.4	0.2

[a]The percentage difference between the coarsest and the finest grids.
[1*]The Euler number defined as the dimensionless pressure drop
[2*]The Stokes number defined as the dimensionless particle diameter

$$t_{res}=\frac{V}{Q} \quad (14)$$

where V is cyclone volume, and Q is the gas volume flow rate. The time step of 10^{-4} s is used in the simulations.

4. Solver Setting

The gas flow simulations in the cyclones were carried out with commercial software Ansys-Fluent 19. The governing transport equations were solved numerically using the Finite Volume Method

Table S3. The used discretization schemes in the simulations

Numerical setting	Scheme
Pressure discretization	PRESTO!
Pressure velocity couple	SIMPLEC
Momentum discretization	QUICK
Turbulent kinetic energy	Second Order Upwind
Turbulent dissipation rate	Second Order Upwind
Reynolds Stress	First Order Upwind

(FVM). Karagoz and Kaya [5] tested different discretization approaches in their study. They reported suitable discretization for high swirl flows in cyclones. Their suggested numerical schemes were used in the present study. Table S3 shows the schemes used in the simulations. The SIMPLC (semi-implicit method for pressure-linked equations-consistent) algorithm was used for discretizing pressure-velocity coupling. The PRSTO (pressure staggering option) scheme was used for pressure interpolation. The momentum equations were discretized using the QUICK quadratic upwind differencing scheme. For the turbulence kinetic energy equation, the second-order upwind was used. The turbulence dissipation rate and the Reynolds stress transport equations were discretized using the first-order upwind in the present simulation.

REFERENCES

1. L. Schiller and Z. Naumann, *Z. Ver. Deutsch. Ing.*, **77**, 318 (1935).
2. Y. I. Oka, K. Okamura and T. Yoshida, *Wear*, **259**, 95 (2005).
3. Y. I. Oka and T. Yoshida, *Wear*, **259**, 102 (2005).
4. A. J. Hoekstra, *Gas flow field and collection efficiency of cyclone separators*, Delft University of Technology, TU Delft (2000).
5. I. Karagoz and F. Kaya, *Int. Commun. Heat Mass Transf.*, **34**, 1119 (2007).